AGU PUBLICATIONS

JGR

Journal of Geophysical Research: Atmospheres

RESEARCH ARTICLE

10.1002/2013JD019880

Key Points:
- Orographic snowfall enhancement near the summit region
- Preferred snow deposition on leeward slopes
- Snow drift affects reflectivity patterns observed by radar

Correspondence to:
R. Mott,
mott@slf.ch

Citation:
Mott, R., D. Scipión, M. Schneebeli, N. Dawes, A. Berne, and M. Lehning (2014), Orographic effects on snow deposition patterns in mountainous terrain, *J. Geophys. Res. Atmos.*, *119*, 1419–1439, doi:10.1002/2013JD019880.

Received 21 MAR 2013
Accepted 3 JAN 2014
Accepted article online 7 JAN 2014
Published online 4 FEB 2014

Orographic effects on snow deposition patterns in mountainous terrain

R. Mott[1], D. Scipión[2,3], M. Schneebeli[4], N. Dawes[1], A. Berne[2], and M. Lehning[1,5]

[1]WSL Institute for Snow and Avalanche Research SLF, Davos, Switzerland, [2]Environmental Remote Sensing Laboratory, School of Architecture and Civil Engineering, École Polytechnique Federale de Lausanne, Lausanne, Switzerland, [3]Radio Observatio de Jicamarca, Instituto Geofisico del Perú, Lima, Peru, [4]Federal Office of Meteorology and Climatology MeteoSwiss - Radar, Satellites and Nowcasting, Locarno, Switzerland, [5]Laboratory of Cryospheric Sciences, School of Architecture and Civil Engineering, École Polytchnique Federale de Lausanne, Lausanne, Switzerland

Abstract Orographic lifting of air masses and other topographically modified flows induce cloud and precipitation formation at larger scales and preferential deposition of precipitation at smaller scales. In this study, we examine orographic effects on small-scale snowfall patterns in Alpine terrain. A polarimetric X-band radar was deployed in the area of Davos (Switzerland) to determine the spatial variability of precipitation. In order to relate measured precipitation fields to flow dynamics, we model flow fields with the atmospheric prediction model "Advanced Regional Prediction System." Additionally, we compare radar reflectivity fields with snow accumulation at the surface as modeled by Alpine3D. We investigate the small-scale precipitation dynamics for one heavy snowfall event in March 2011 at a high resolution of 75 m. The analysis of the vertical and horizontal distribution of radar reflectivity at horizontal polarization and differential reflectivity shows polarimetric signatures of orographic snowfall enhancement near the summit region. Increasing radar reflectivity at horizontal polarization over the windward slopes toward the crest and downwind decreasing reflectivity over the leeward slopes is observed. The temporal variation of the location of maximum concentration of snow particles is partly attributed to the effect of preferential deposition of snowfall: For situations with strong horizontal winds, the concentration maximum is shifted from the ridge crest toward the leeward slopes. Qualitatively, we discuss the relative role of cloud microphysics such as the seeder-feeder mechanism versus atmospheric particle transport in generating the observed snow deposition at the ground.

1. Introduction

Orography plays an important role in defining the rain and snowfall distribution at different scales, ranging from global to regional and very small scales of tens of meters. On each scale, however, different processes can be identified to be the main driving factors for the spatial variability of precipitation as well as altitudinal gradients of snow deposition in mountains [*Kuhn*, 2003; *Blanchet et al.*, 2009; *Grünewald and Lehning*, 2011; *Lehning et al.*, 2011]. On large scales, ambient atmospheric circulations drive orographic precipitation [*Stoelinga et al.*, 2013] and for high mountains the precipitation is likely to be greater on the windward slopes of mountains [*Houze*, 2012]. On a much smaller scale, the effects of the near-surface flow field on particle trajectories can cause a shift of maximum precipitation toward the leeward slopes [*Choularton and Perry*, 1986; *Colle*, 2004; *Zängl*, 2008; *Orlandini and Lamberti*, 2000; *Lehning et al.*, 2008; *Mott et al.*, 2010; *Dadic et al.*, 2010a; *Winstral et al.*, 2013]. The spatial variability of precipitation in mountainous terrain can be also driven by microphysical processes such as the seeder-feeder mechanism causing locally enhanced rain and snowfall rates [*Choularton and Perry*, 1986; *Dore and Choularton*, 1992; *Zängl*, 2008; *Zängl et al.*, 2008; *Stoelinga et al.*, 2013]. In the case of a seeder-feeder process, seeding precipitation particles produced by a large-scale storm fall through the orographically produced feeder cloud. As the cloud condensate is efficiently collected by the seeding precipitation particles, more precipitation can be locally generated than the sum of what might have been generated separately by the large-scale and the orographic cloud [*Stoelinga et al.*, 2013].

There are a large number of studies relating small-scale precipitation patterns to air flow dynamics and/or microphysical processes in mountainous terrain [*Anquetin et al.*, 2003; *Colle*, 2004; *Anders et al.*, 2007; *Zängl*, 2007a, 2007b, 2008; *Zängl et al.*, 2008; *Lehning et al.*, 2008; *Minder et al.*, 2008]. Some of these studies [*Choularton and Perry*, 1986; *Dore and Choularton*, 1992; *Medina and Houze*, 2003; *Colle*, 2004; *Houze and*

Medina, 2005; *Purdy et al.*, 2005; *Zängl*, 2007b, 2008; *Zängl et al.*, 2008] showed that the orographic enhancement of precipitation due to the seeder-feeder mechanism [*Bergeron*, 1965; *Colle*, 2004; *Colle et al.*, 2013; *Stoelinga et al.*, 2013] is a key process in producing local precipitation maxima over mountains.

While the orographic enhancement of rainfall has been extensively studied by numerical and field studies, a smaller number of studies explicitly investigated the orographic enhancement of precipitation [*Choularton and Perry*, 1986; *Rauber et al.*, 1986; *Rauber*, 1987; *Dore and Choularton*, 1992; *Minder et al.*, 2008] during a winter storm. Based on numerical studies, they predicted snowfall enhancement due to seeder-feeder mechanism to be even larger than the enhancement of rain. These numerical studies, however, could not be verified by measurements.

Analyzing precipitation patterns governed by orographic enhancement, *Dore and Choularton* [1992], *Zängl* [2008], and *Zängl et al.* [2008] argued that advecting winds cause a downstream drift of the precipitation maxima toward the leeward slopes of mountains. The advection effect was found to be particularly pronounced for snow particles because they have a lower fall velocity than raindrops [*Colle*, 2004; *Zängl*, 2007a]. Due to their higher terminal velocity, the advection effect is less strong for rimed and aggregate snow crystals, which are typically generated by the seeder-feeder mechanism [*Houze and Medina*, 2005]. *Zängl* [2008] and *Zängl et al.* [2008] also explained the spatial distribution of precipitation by convergent and divergent hydrometeor trajectories which are related to the structure of vertical wind speed.

Lehning et al. [2008] introduced the concept of preferential deposition of snow as the phenomenon of particle - flow interaction close to the ground. They described a preferred deposition of snowfall in leeward slopes of mountains purely as a function of the mean near-surface flow field without any effects of microphysical processes. Assuming a horizontal homogenous precipitation rate as an upper boundary condition, the concept is based on the assumption that the particle deposition velocity varies with the mean flow and turbulence field and is thus influenced by convergent and divergent flows as well as by mean horizontal and vertical wind velocities within the atmospheric boundary layer. Near-surface flow acceleration and updrafts cause reduced deposition velocities for snow during precipitation on windward slopes of mountain ridges. In contrast, flow deceleration and flow separation promote enhanced deposition of snow on leeward slopes. This interaction between topographically induced flow field modifications and the precipitation particle distribution causes a spatially varying deposition of precipitation. Further studies investigated the link between the spatial distribution of snow depths and wind-induced processes and suggested that preferential deposition is an important process controlling the small-scale spatial distribution of snow accumulation in Alpine terrain [*Mott et al.*, 2010, 2011] and on Alpine glaciers [*Mott et al.*, 2008; *Dadic et al.*, 2010a, 2010b].

Scipión et al. [2013] compared the seasonal small-scale spatial variability in alpine snowfall measured by a weather radar with a range resolution of 75 m with seasonal snow accumulation measured at the ground. They conclude that the small-scale variability of snow depth on the ground cannot be explained by the spatially distributed snowfall seen by the radar because additional wind-induced processes control the snow distribution on the ground. In our study, we use a novel data set which allows us to investigate the orographically induced snowfall distribution at a very small scale (smaller than 1 km). We aim to identify polarimetric signatures of the main processes driving small-scale snowfall and snow deposition patterns in Alpine terrain. Based on earlier studies [*Choularton and Perry*, 1986; *Dore and Choularton*, 1992; *Lehning et al.*, 2008; *Mott and Lehning*, 2010; *Dadic et al.*, 2010a, 2010b; *Zängl*, 2007b], we expect the snowfall field seen by the radar to be affected by the interaction between microphysical processes and the mean flow field characteristics. We aim to demonstrate the difference between the spatial patterns of snowfall rates seen by the radar at hundreds of meters above the ground and small-scale snow deposition fields at the ground driven by the near-surface boundary layer flow.

This paper is organized as follows. Section 2 presents a description of methods and data. In section 3 we present observational and numerical results. We first present the dynamical aspects of the airflow over the local orography at different scales. In the second part of the results we show the horizontal and vertical distribution of radar reflectivity at horizontal polarization and differential reflectivity for one snowfall day. Here we use the combination of those polarimetric variables to describe snowfall patterns and to distinguish between crystals of different microphysical origins. Similar to other recent studies [*Wolde and Waldi*, 2001; *Moisseev et al.*, 2009; *Plummer et al.*, 2010; *Williams et al.*, 2011], the analysis of microphysical origins of the observed polarimetric signatures is only based on the radar signal. We are thus only offering a hypothesis about possible dominant growth mechanisms of precipitation particles (e.g., aggregation and

riming). We finally present an analysis of polarimetric signatures of particle-flow interactions. In section 4 we present a discussion on the observational and numerical results. In particular, we discuss the relative importance of driving processes causing the observed snowfall distribution at higher atmospheric levels and their potential contribution to the final snow deposition patterns at the ground. Here we focus separately on the pure particle-flow interactions close to the terrain surface driven by the topographically modified near-surface flow field and the interactions between microphysics with large- and small-scale dynamical aspects of the orographic flow. Finally, we provide snow concentration and snow deposition fields which would theoretically arise from the impact of snowfall enhancement, preferential deposition of snowfall, and the combination of both processes.

2. Methods and Data

2.1. Site Description and Radar Measurements

A mobile dual-polarized Doppler X-band radar was deployed on the Ischalp (2133 m above sea level (asl)), in the region of Davos (Figure 1a) for the winter seasons 2009/2010 and 2010/2011. The inner-alpine study site has a domain size of approximately 30 km^2 (Figure 1a) and is located on the opposite side of the valley including the Wannengrat experimental site, where several studies on snow depth variability have been completed in recent years [*Mott et al.*, 2010; *Grünewald and Lehning*, 2011; *Groot Zwaaftink et al.*, 2011; *Schirmer et al.*, 2011]. Mountain peaks locally range between 2500 and 2850 m. The altitude difference of the mountains peaks versus the surrounding terrain typically varies between 200 and 1000 m. Radar data were obtained in polar coordinates with a 1.1° angular resolution and a range resolution set to 75 m. In order to combine radar data to numerical results, radar data were projected from polar to Cartesian coordinates. The radar operates at a frequency of 9.41 GHz. Continuous radar measurements were performed in a 5 min cycle. The radar sequence of plane position indicator (PPI) was adjusted to different elevations (Figure 1b). As measurements at lower levels (0°, 2°, and 5°) are strongly contaminated by ground clutter returns and do not cover the atmosphere above pronounced peaks, we analyzed the PPI at an elevation of 9° in order to investigate the horizontal distribution of polarimetric data. Additionally, polarimetric radar data from the 14°, 20°, and 27° level scans were used to analyze proxies for vertical polarimetric profiles. In order to produce these profiles, data were calculated directly from polar coordinates. PPI scans were selected at particular elevation ranges as distance from the radar beam height at ground level. Finally, radial distances were converted to corresponding elevation, and the polarimetric data were averaged over an angular resolution of 15° and plotted for the different elevations.

We analyzed the radar reflectivity at horizontal polarization (Z_H), the differential reflectivity (Z_{DR}), and the mean radial velocity (V_H) for one major snowfall day in March 2011. Note that mean values of Z_H were calculated from the linear radar reflectivity factor ($mm^6\ m^{-3}$) and were then converted into the common logarithmic radar reflectivity factor (dBZ). Z_{DR} defines the ratio between the radar reflectivity in horizontal and vertical polarization and is independent from particle concentration. We chose the snowfall event on 17 March 2011 as a representative case study because of good data quality, high precipitation rates, and strongly varying wind conditions (Figure 5). No measurements of the spatial distribution of snow depths after the snowstorm are available.

We applied a signal-to-noise ratio threshold of 5 dB to remove low signal returns. In order to remove any residual ground clutter echoes from the data, a hydrometeor classification scheme was applied, as described by *Shuur et al.* [2003] and *Park et al.* [2009]. More detailed specifications of the mobile X-band radar can be found in *Muth et al.* [2012], *Scipión et al.* [2013], and *Schneebeli et al.* [2013].

2.2. Numerical Modeling

Modeled fields of total hourly precipitation and air temperature were obtained from a numerical weather forecast model COSMO-2, which is nonhydrostatic and fully compressible [*Schättler and Barbu*, 2010]. Precipitation and temperature fields are shown for a grid resolution of 2.2 km. COSMO-2 is based on COSMO and is used operationally by the Federal Office of Meteorology and Climatology MeteoSwiss since 2008.

In order to demonstrate the effect of the topographically modified flow field near the surface on the snow deposition field, we modeled small-scale flow fields with the meteorological prediction model Advanced Regional Prediction System (ARPS) [*Xue et al.*, 2001]. Flow fields were modeled at a horizontal resolution of 25 m. As has already been described in previous publications [*Mott and Lehning*, 2010; *Groot Zwaaftink et al.*, 2011], a library of mean flow fields has been developed that can save computational time. The vertical

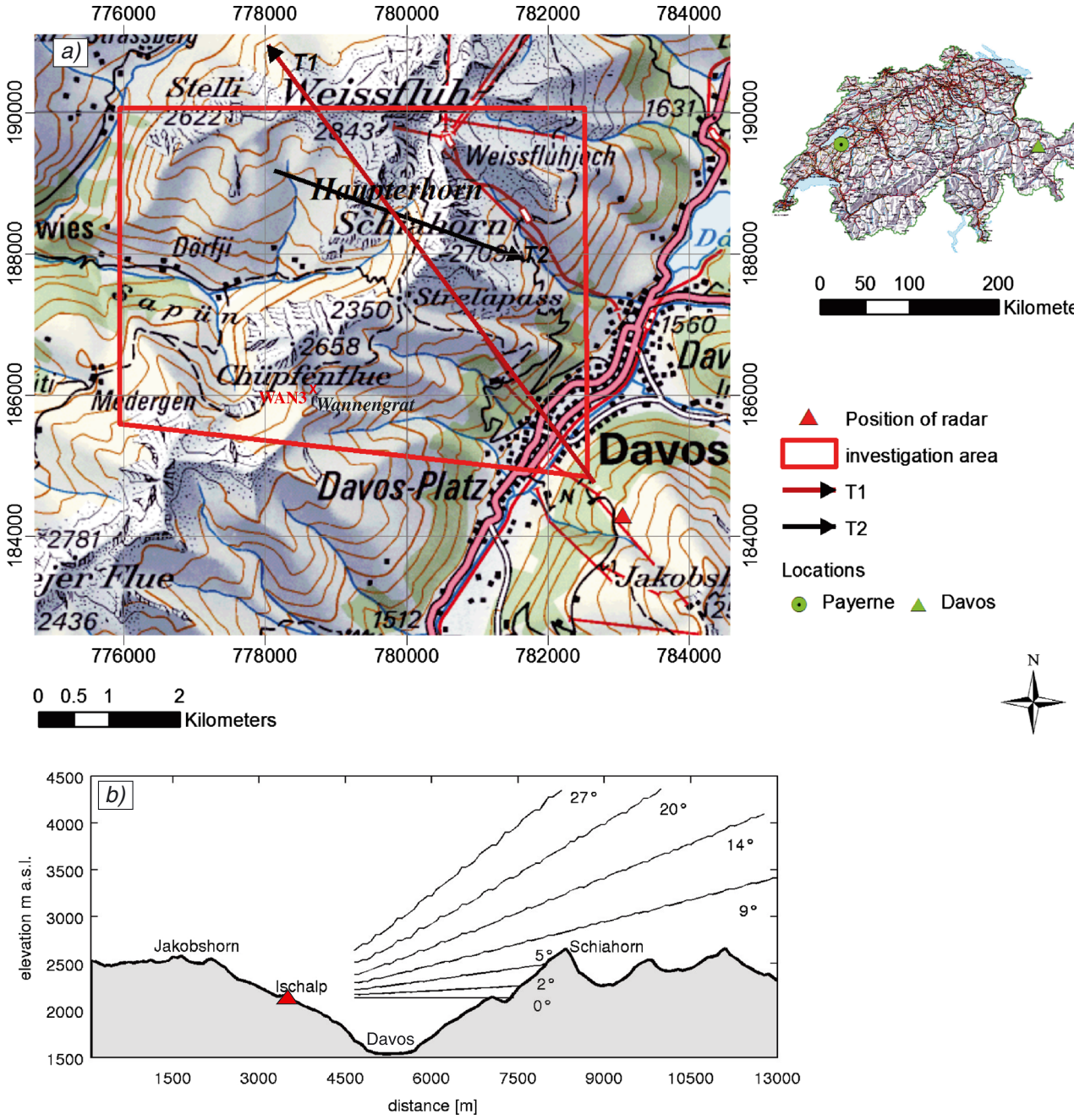

Figure 1. (a) Study site and position of radar. The *x* and *y* axes give Swiss coordinates in meters. Black arrows indicate the direction of transects T1 and T2 with the head of the arrow indicating the end of the transect; (b) radar measurement setup and topographic transect along T1. Note that radar measurements only for the 9° level and above have been used in this study. (base map: Pixelkarte PK 25 ©2009 swisstopo (dv033492)).

profiles of the initialized atmospheric boundary layer (ABL) were assumed to be slightly stably stratified (Figure 3c). The Brünt-Vaisala frequency of 0.0076 s^{-1} is consistent with the static stability calculated from the atmospheric sounding (Figures 3a and 3b) measured at 1200 UTC on 17 March 2011 in Payerne (Switzerland), which is located approximately 200 km to the west of Davos. We also note that Payerne is located at much lower elevation (456 m asl) than the investigation area (1600–2800 m asl). Due to considerable differences in location and elevation, we simplified the atmospheric profile by applying the static stability calculated for the first 500 m aboveground to the entire profile. This simplification is assumed to be adequate as we only calculate the adaptation of the near-surface flow field to the local orography. We

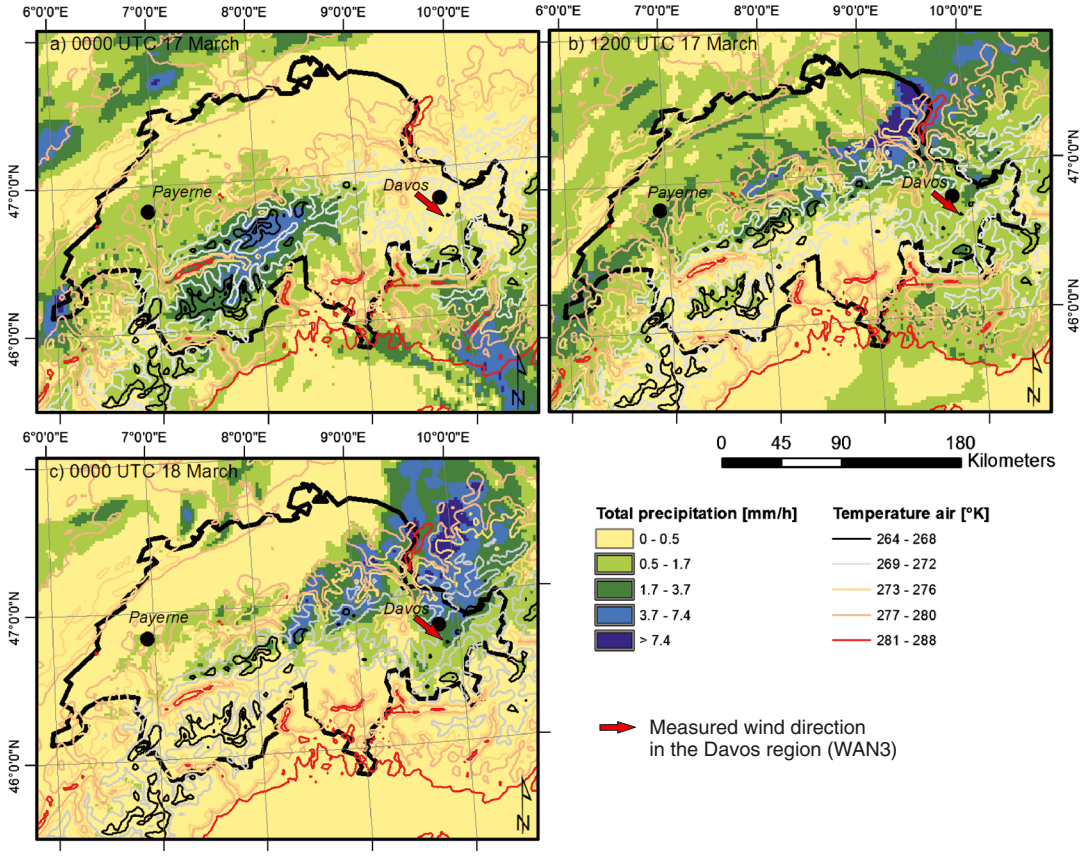

Figure 2. Modeled fields of total hourly precipitation and air temperature with COSMO2 for (a) 0000 UTC on 17 March, (b) 1200 UTC on 17 March, and (c) 0000 UTC on 18 March. The arrow indicates predominant wind direction in the region of Davos measured at WAN3 1.

do not aim to simulate large- and regional-scale flow characteristics. The near-surface air temperature was obtained from the meteorological station WAN3 located in the Wannengrat area (Figure 5). As discussed in earlier studies [*Mott et al.*, 2010; *Schirmer et al.*, 2011], the prevailing wind direction is northwest, which is the primary influence on snow depth distribution that is observed in this region. As the meteorological station WAN3 (Figure 1a) also recorded a northwest wind direction during the entire investigation period, flow fields were only calculated for this wind scenario. Based on wind velocity measurements, the flow fields were initialized with wind velocities between 1.5 m s^{-1} and 6 m s^{-1}, resulting in six different flow fields. *Mott et al.* [2010] demonstrated that predominant snow deposition features can be captured for the Wannengrat area using a library of mean flow fields.

Modeled flow fields are used as an important input for modeling the interaction between snow particles and the small-scale atmospheric boundary layer flow as well as the final snow deposition at the ground. We applied the snow surface process model Alpine3D to calculate snow deposition at the ground caused by preferential deposition of precipitation [*Lehning et al.*, 2008; *Mott and Lehning*, 2010; *Dadic et al.*, 2010a]. The drift module consists of a saltation and a suspension layer [*Clifton and Lehning*, 2008]. The concentration in the saltation layer is for standard applications used as the bottom boundary condition for the suspension layer. However, saltation is switched off for the current application such that deposition and not redistribution is considered. Initialized spatially homogeneous snowfall rates form the top and lateral boundary conditions for the suspension layer. Within the suspension layer, snow transport by suspension and preferential deposition of precipitation are calculated based on the three-dimensional flow field simulated with ARPS. Modeled flow fields obtained from ARPS are chosen as an hourly input using a classification scheme based on the hourly wind velocity and direction measured at WAN3.

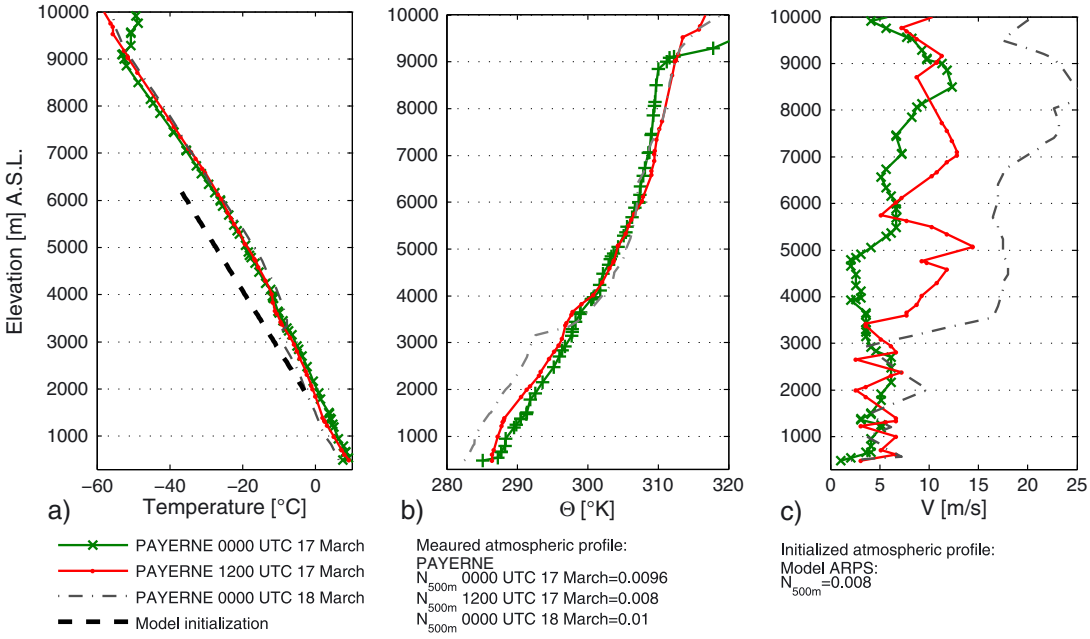

Figure 3. (a) Profiles of measured air temperatures obtained from atmospheric soundings in Payerne, Switzerland, at 0000 and 1200 UTC on 17 March 2011, at 0000 UTC on 18 March 2011, and of initialized air temperatures. (b) Measured potential air temperatures θ obtained from atmospheric soundings in Payerne, Switzerland, at 0000 and 1200 UTC on 17 March 2011 and at 0000 UTC on 18 March 2011. Brünt-Vaisala frequency N was calculated for the first 500 m aboveground. (c) Measured wind velocity V obtained from atmospheric soundings in Payerne, Switzerland, at 0000 and 1200 UTC on 17 March 2011 and at 0000 UTC on 18 March 2011. Data are provided by the University of Oklahoma.

3. Results

3.1. The Flow Field

3.1.1. The Synoptic Setting

Fields of total hourly precipitation and air temperature obtained from the Swiss operational weather forecast model COSMO-2 [*Schättler and Barbu*, 2010] is shown in Figure 2 for 0000 UTC and 1200 UTC on 17 March and 0000 UTC on 18 March. Precipitation fields show the passage of a cold front over Switzerland with an intensive precipitation in the region of Davos at 1200 UTC on 17 March and 0000 UTC on 18 March. The predominant wind direction measured at the meteorological station WAN3 (Davos) was northwest for the entire time period of 24 h. Atmospheric soundings (Figure 3) measured at station Payerne (Figure 1a) are shown for 0000 UTC and 1200 UTC on 17 March and 0000 UTC on 18 March during the time period when the precipitating systems passed that region. Proxies for vertical polarimetric profiles of radial velocities measured above the Schiahorn ridge are presented for 0000 UTC on 17 March to 0000 UTC on 18 March 2011 in Figure 4. Both the atmospheric soundings launched 200 km west to Davos (Figure 3c) as well as the polarimetric profile of radial velocities measured in the region of Davos (Figure 4) indicate the development of a strong shear layer between approximately 3000–4000 m and a low-level layer of apparently retarded flow. The retarded low-level flow appears to be bounded above by strong shear, separating the lower atmospheric layer from the higher levels (Figure 4). The strength of the wind shear increased during the snowfall event. The vertical profiles and the calculated Brunt-Vaisala frequency indicates that the atmosphere was slightly stable throughout most of the lowest 7000 m (Figures 3a and 3b). At 0000 UTC on 18 March, a layer of increased stability near the top of the wind sheared layer was present between 3000 and 3500 m (Figure 3b). The flow within the first 500 m aboveground was more stable at the beginning of the cold front passage, became less stable at 1200 UTC, and returned to more stable conditions at 0000 UTC on 18 March (Figure 3). While the air temperature decreased when the frontal system passed Payerne, the wind velocities increased, which is consistent with measured air temperatures and wind velocities at WAN3 in the Davos region (Figure 5).

3.1.2. The Small-Scale Flow Field Characteristics

Modeled and measured mean radial velocities at radar measurement height are compared in Figure 6. The prevailing wind was northwest, perpendicular to local orography for the entire snowfall event. Although modeled radial velocities show a lower spatial variability than measured ones, the general patterns of flow acceleration and deceleration caused by the complex terrain are well captured by ARPS

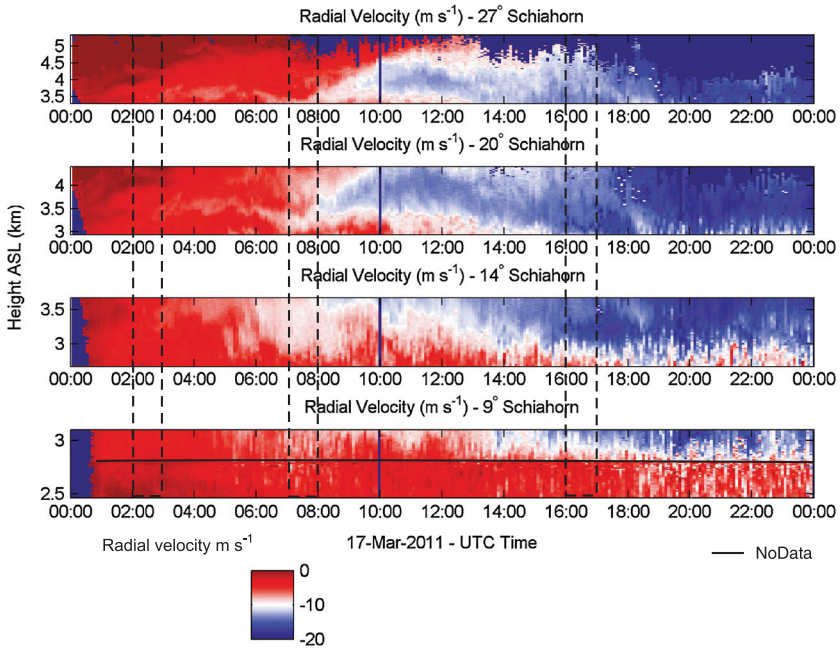

Figure 4. Time series of proxy for vertical profiles of radial wind velocity (V_H) above the Schiahorn summit at 0000 UTC on 17 March to 0000 UTC on 18 March 2011 . Black boxes indicate the time periods discussed in Figures 9a–9f. Data were averaged over an angular sector scan of 15°. Note that NoData values are due to the ground clutter in this area.

(Figures 6a–6c). Measured radial velocities along the transect T1 (Figure 6c) during this single precipitation event show strong flow acceleration at the ridge crests of the Haupterhorn and the Schiahorn and deceleration on the leeward slopes of the mountain ridges indicating flow separation on these slopes. These observed flow structures suggest an unblocked flow regime at those atmospheric levels, which is a sign of the presence of a weak static stability. The weak static stability is also confirmed by atmospheric soundings (Figure 3). Stronger static stability would result in a blocked flow regime at lower levels and less flow acceleration on windward slopes. Results of this study are thus only valid for this particular stability regime, which is, however, typical for winter snowfall events. Accordingly, the numerical model was initialized with a slightly stable atmosphere (see section 2.2). For the purpose of investigating possible small-scale effects of air flow dynamics on small-scale snowfall patterns, we shall only consider modeled mean flow field characteristics for northwest inflow conditions and assume a slightly stable atmosphere.

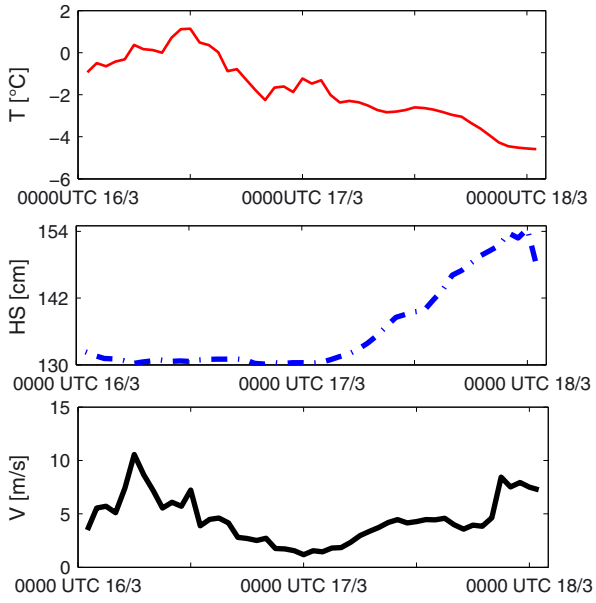

Figure 5. Time series of hourly air temperature T, snow depth HS, and hourly wind velocity V measured at Wannengrat station WAN 3 (see Figure 1) from 0000 UTC on 16 March to 0000 UTC on 18 March 2011.

The spatial distribution of the vertical wind velocity and surface-normal wind velocity modeled for the prevailing wind direction northwest is shown in Figure 7. Positive values indicate updraft zones, and negative values indicate downdraft zones. The surface-normal wind velocity should be a direct measure for lifting or sinking of air parcels relative to the topography [*Dadic et al.*, 2010a]. Numerical results suggest small-scale patterns of updrafts and downdrafts at the lowest numerical level aboveground (Figures 7a and 7b), which is about

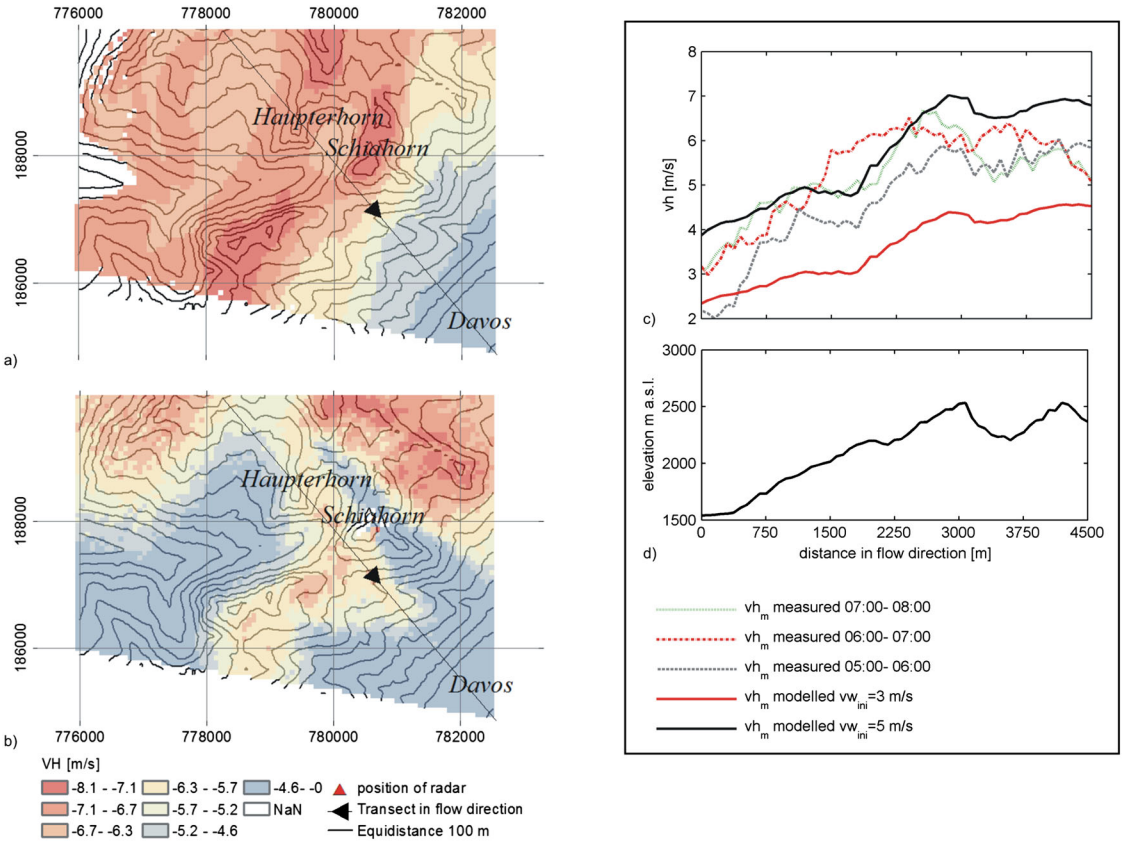

Figure 6. Spatial distribution of (a) modeled (initialized wind velocity = 5 m/s) and (b) measured (0600–0700 UTC on 17 March 2011) mean radial velocity V_H. The location of the transect T1 of (c) modeled radial velocity (wind velocity = 5 m/s and 3 m/s) and measured mean hourly radial velocity V_H (0500–0800 UTC on 17 March 2011) is indicated in Figures 6a and 6b. The head of the arrow marks the endpoint of the transect as shown in Figures 6c and 6d. The *x* and *y* axes indicate Swiss coordinates in meters. (d) Transect of topography. (basemap: Pixelkarte PK 25 ©2009 swisstopo (dv033492)).

3 m aboveground for ridges and summits. For northwest wind scenarios, the ridge between Chüpfenflue and Schiahorn forms a transition zone between the larger-scale updraft zone to the west and the downdraft zone to the east (Figures 7a and 7c). The strongest near-surface updraft zones were modeled for the windward slopes of Chüpfenflue, Strelapass, and Schiahorn. The strongest downdraft zone is located on the leeward slope of the Schiahorn. The lifting of air masses on the windward side of the ridge causes a compression of streamlines close to the ridge crest, which in turn leads to flow acceleration in those areas (Figure 6). Flow deceleration and streamwise flow convergence is typically found downwind of the ridge crest on the leeward slopes (Figure 6), where flow separation presumably occurs. The simulated mean flow at the radar measurement height shows that vertical wind velocities are very small at the height seen by the radar. Although the vertical wind velocities are still positive at the radar measurement height, surface-normal wind velocities are negative on steep windward slopes and positive on steep leeward slopes.

3.2. Snowfall Patterns and Particle Types

We present transects of mean radar reflectivity at horizontal polarization (Z_H) and differential reflectivity (Z_{DR}) obtained from the 9° level scan for one snowfall day on 17 March 2011 (Figure 8) for a time period of 20 h, during which time a frontal system passed over the region of Davos. Transect T2 crosses the most pronounced peak of the region, the Schiahorn (Figure 9). Z_{DR} is the weighted mean axis ratio of the particle size distribution. Values of differential reflectivity (Z_{DR}) depend on the size, shape, orientation, density, and the phase composition of hydrometeors but are not affected by the particle concentration [*Andrić et al.*, 2013]. Large particles contribute more to the reflectivity than small particles do [*Schneebeli et al.*, 2013].

Along T2, the distance of the radar beam height to the ground ranges between 200 m and 850 m. The minimum distance of 200 m can be found above the Schiahorn peak (Figure 8i). The selected time period is characterized by air temperatures ranging between −3°C around midday and −4°C in the afternoon (measured at WAN3), strong snowfall, and a gradual change from low to high radial velocities (Figure 5).

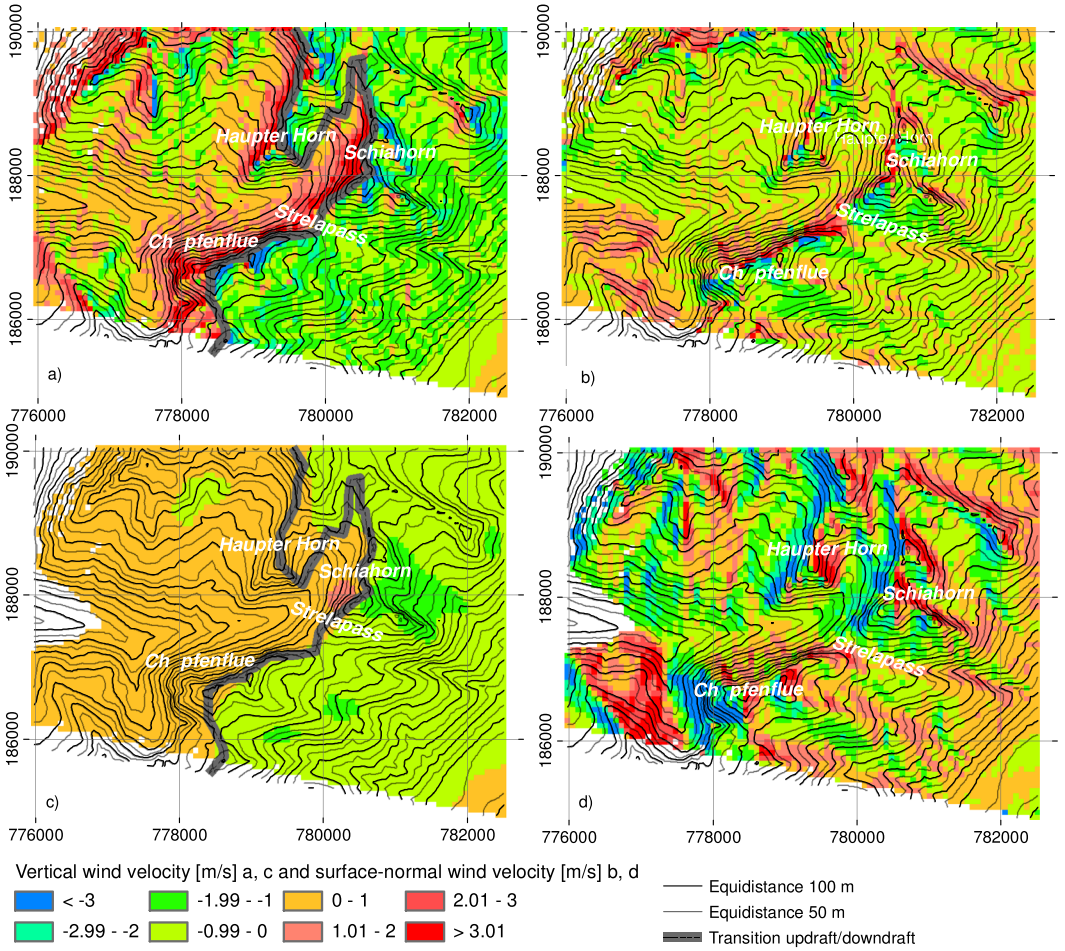

Figure 7. Vertical wind velocity (m/s) modeled (a) at ground level and (c) for the height seen by the radar (see also Figure 1c). Surface-normal wind velocity (m/s) modeled (b) at ground level and (d) for the height seen by the radar. The transition zone between updraft and downdraft zone is indicated by a red line. The *x* and *y* axes indicate Swiss coordinates in meters.

In addition to the transects shown in Figure 8, the horizontal distribution of hourly mean Z_H and Z_{DR} are presented in Figure 9 for the specific scenarios discussed in the text below. In order to analyze the vertical distribution of Z_H and Z_{DR}, the time series of the proxy for vertical profiles of Z_{DR} and Z_H, gained from radar measurements at 9°, 14°, 20°, and 27° levels are presented for the 20 h time period in Figure 10. These profiles were produced from data measured within an angular sector above the Schiahorn summit. All measurements were located above the melting layer during the entire time period.

The time period 0000–0500 UTC on 17 March is characterized by low wind velocities. Z_H appears to be spatially homogeneous over the windward side but slightly increases downwind over the leeward side of the Schiahorn ridge crests (Figure 9a). The homogeneous distribution of Z_{DR} along the transect (Figures 8a, 8b, and 8j) indicates the consistent particle characteristics across the mountain ridge. Since particles along the transect are assumed to be of similar particle size distribution, Z_H can be assumed to be a direct measure for snow particle concentration in the air. Proxies for vertical Z_H and Z_{DR} profiles at 0200–0300 UTC on 17 March indicate a rather homogenous vertical distribution of particle concentration, shape, and size without significant layering (Figure 10). The joint occurrence of low values of reflectivity (approximately 10 dBZ) and high Z_{DR} values (> 0.9 dB) observed for the whole profile are comparable to values found in previous studies [*Houze and Medina*, 2005; *Andrić et al.*, 2013] for dry snow particles. A slight decrease of differential reflectivity with decreasing altitude (in downwind direction, Figures 8b and 10) can be attributed to lower temperatures at higher altitudes inducing the formation of more pristine ice crystals such as plates and columns that cause a higher Z_{DR} signal [*Schneebeli et al.*, 2013]. The pristine crystals begin to aggregate at

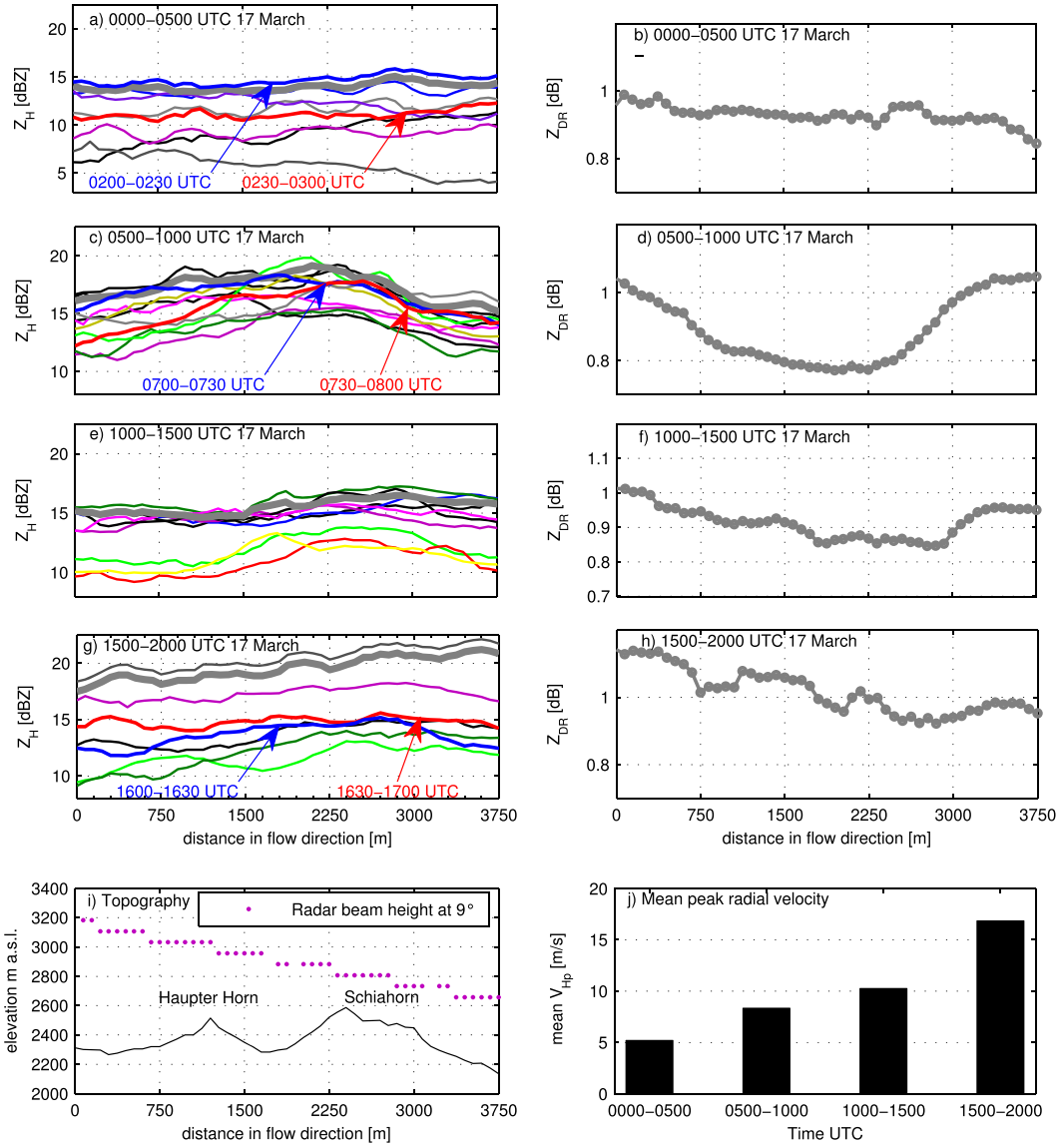

Figure 8. Mean radar reflectivity at horizontal polarization (Z_H) and mean differential reflectivity (Z_{DR}) along transect T2 on 17 March for time periods (a, b) 0000–0500 UTC, (c, d) 0500–1000 UTC, (e, f) 1000–1500 UTC, and (g, h) 1500–2000 UTC on 17 March 2011. While Z_H values were averaged over 30 min (colored lines) and over the respective time period of 5 h (bold line), Z_{DR} values were only averaged over the four time periods of 5 h. Transects for time periods that are further discussed in Figure 9 are labeled. (i) Topography of T2 and (j) the peak radial velocities (V_{Hp}) averaged over respective time periods shown in Figures 8a–8h. Location of transect T2 is shown in Figure 1.

lower altitudes forming larger though less dense and more spherical particles, which results in a decrease of Z_{DR} and in an increase of Z_H [*Andrić et al.*, 2013].

The time period 0500–1000 UTC features moderate to high wind velocities. The reflectivity curves show a high temporal and spatial persistence of mean reflectivity curves over several hours (bold lines, Figures 8c and 8e). The mean Z_H signals for the time period 0500–1000 UTC were increasing over windward slopes toward the ridge crest and were decreasing over leeward slopes in the downwind direction. A very distinct peak of Z_H can be observed near the summit of Schiahorn (see also Figure 9c). Moreover, the values of Z_{DR} show clear spatial patterns. The radar observed a region of low differential reflectivity near the Schiahorn crest (see also Figure 9d) that coincides with the area of high Z_H (Figure 9c). The observed spatial variability indicates strong differences in particle types. Vertical polarimetric profiles at 0700–0800 UTC (Figure 10) show a low-level layer of high Z_H (25–30 dBZ) and low Z_{DR} signals (0.4–0.6 dB). Above this layer, Z_{DR} values get significantly larger, ranging from 1dB to 1.5 dB. The high Z_H and low Z_{DR} values near the ground suggest that

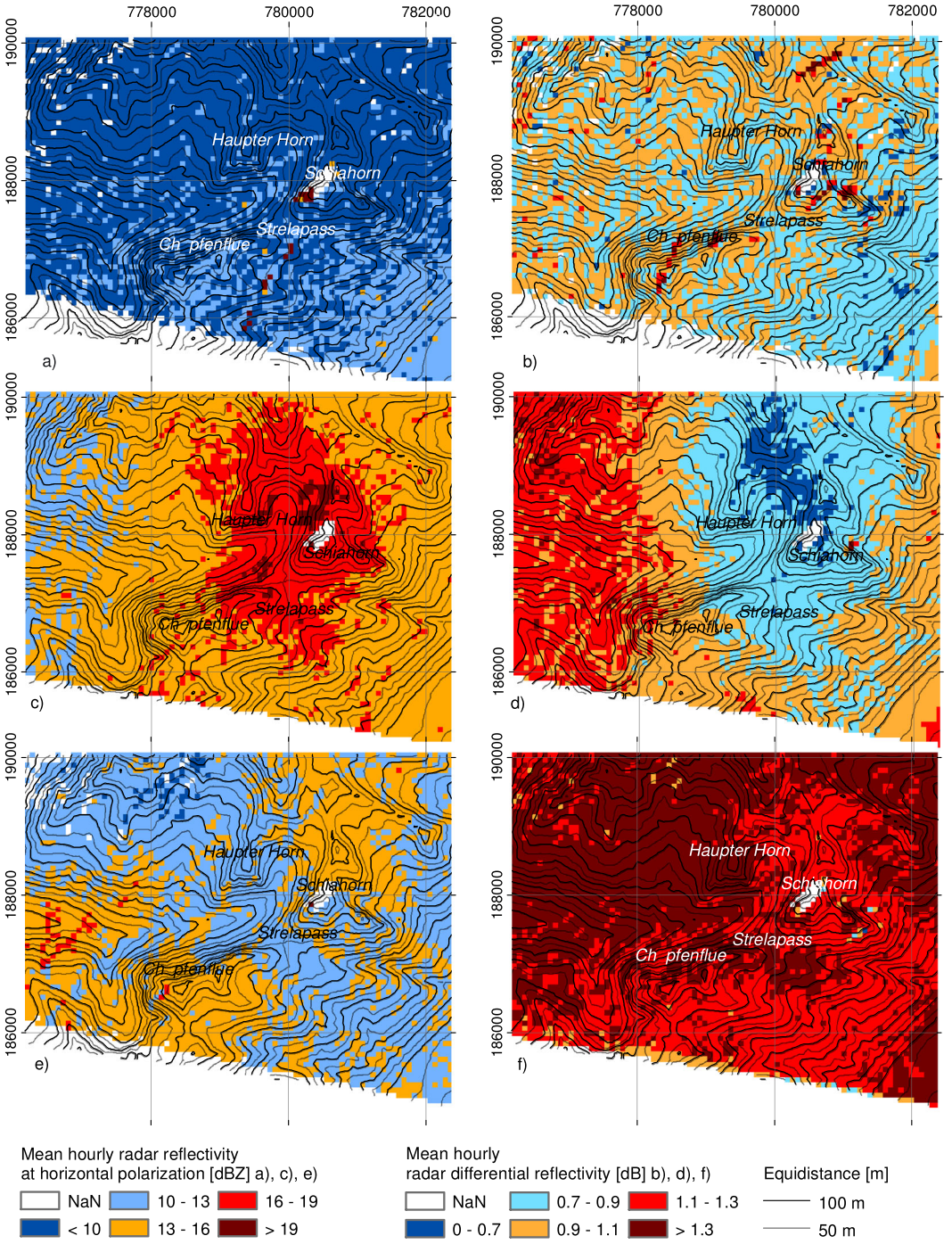

Figure 9. Mean radar reflectivity at horizontal polarization (Z_H) and differential reflectivity (Z_{DR}) averaged over time periods on 17 March 2011 at (a, b) 0200–0300 UTC, (c, d) 0700–0800 UTC, and (e, f) 1600–1700 UTC.

the particles were almost spherical being either large in size or having a large density [*Andrić et al.*, 2013]. If these values are compared to typical values found by other studies [*Bader et al.*, 1987; *Ryzhkov and Zrnić*, 1998; *Wolde and Waldi*, 2001; *Houze and Medina*, 2005; *Williams et al.*, 2011; *Andrić et al.*, 2013], then the measurements indicate the presence of graupel and dry aggregates of snow at lower atmospheric levels. *Bader et al.* [1987] and *Houze and Medina* [2005] found that small or large dry aggregates (including rimed aggregates) retain low values of Z_{DR} as long as they remain dry. The layer of graupel/dry aggregates gets larger around midday reaching a height of approximately 3500 m asl before disappearing at 1600 UTC (Figure 10).

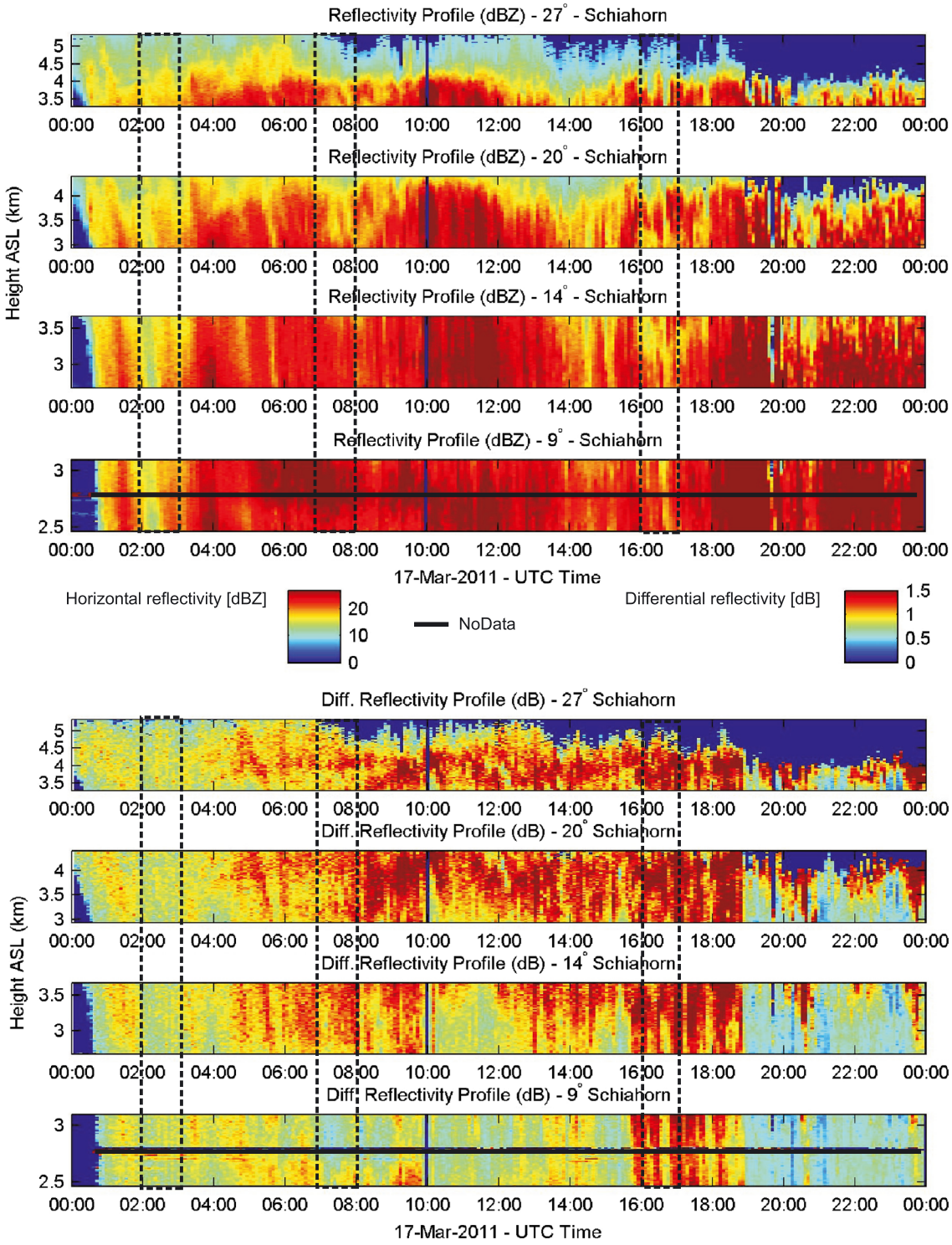

Figure 10. Time series of proxy for vertical profiles of mean radar reflectivity at horizontal polarization (Z_H) and differential reflectivity (Z_{DR}) above the Schiahorn summit at 0000 UTC on 17 March to 0000 UTC on 18 March. Black boxes indicate the time periods discussed in Figures 9a–9f. Data were averaged over an angular sector scan of 15°. Note that NoData values are due to the ground clutter in this area.

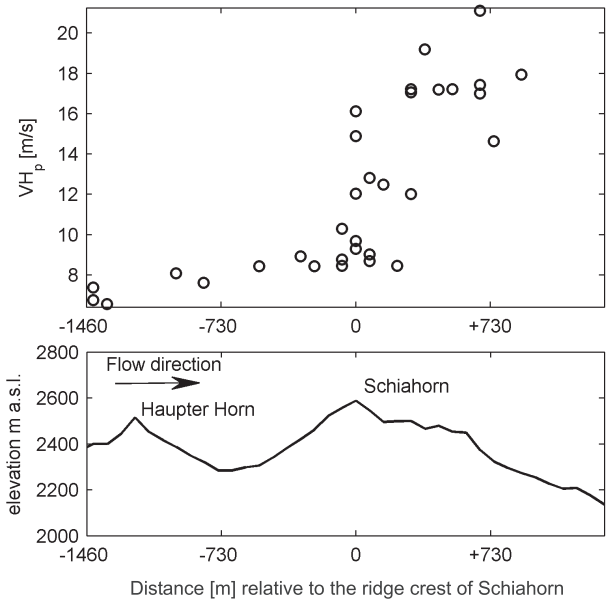

Figure 11. Location of Z_H maximum along T2 is plotted against the peak radial wind velocity (V_{Hp}) measured between 0000 UTC and 2000 UTC within the range of 500 m upwind and 500 m downwind from the ridge crest of the Schiahorn. T2 is crossing the Haupter Horn and the Schiahorn. Pearson's correlation value $r = 0.77$. The location of maximum particle reflectivity (which indicates particle concentration) is shown in distance relative to the ridge crest Schiahorn, which marks 0 at the x axis. Location of transect T2 is shown in Figure 9.

Lower Z_H and higher Z_{DR} values at higher atmospheric levels indicate a layer of nonaggregated snow crystals aloft.

Radar signals later in the day show less pronounced peaks of Z_H above the Schiahorn crest (Figure 9e). While a maximum reflectivity near the ridge crest is still observable between 1000 and 1500 UTC (Figure 8e), only spatial patterns of a slight downwind increase in Z_H near the summit region can be observed later in the afternoon (Figure 9e). Less pronounced spatial patterns of Z_H and low spatial variability in Z_{DR} signals (Figures 8g, 8h, 9e, and 9f) indicate a return to more spatially homogeneous atmospheric conditions. After 1600 UTC the entire profile up to 4000 m asl is dominated by a constant Z_{DR} signal without significant layering (Figure 10).

3.3. Polarimetric Signatures of Peak Concentration Near the Ridge Crest

While spatially homogeneous precipitation rates were observed for low wind velocities (below 5 m/s radial velocity) (Figures 8a and 8j), pronounced peaks of particle concentration were observed close to the Schiahorn ridge crest (Figure 9) for time periods characterized by moderate to high wind velocities (above 5 m/s radial velocity) (Figures 8c, 8e, 8g, and 8j). The location of the maximum is, however, dependent on wind velocity variations. For low to moderate wind velocities (Figures 8c and 8j) the concentration peaks were located close to the ridge crest. For higher wind velocities (Figures 8e, 8g, and 8j), peaks were shifted in the downwind direction toward the leeward slope.

In Figure 11, the location of the precipitation maximum along T2 is plotted against the peak radial wind velocity (V_{Hp}), measured in the range from 500 m upwind to 500 m downwind from the ridge crest of the Schiahorn. As no significant variation in the radar reflectivity as a function of downwind location was observed for very low radial velocities (Figure 8a), these data were not applied to the analysis. This explains the low data density for low radial velocities in Figure 11.

The peak concentration location correlates with peak radial velocity with $r = 0.77$ (Figure 11). The considerable influence of wind velocity on the location of the snowfall maximum with respect to the ridge crest can be explained by an increasing advection of the maximum of snow particle concentration with increasing wind velocity. For low radial velocities the peaks were located above the Haupter Horn or on the windward slope of the Schiahorn (Figure 8b). Most peaks were, however, found around the ridge crest of the Schiahorn. For radial velocities above 10 m/s, strong advection caused a shift in the maximum particle concentration up to 750 m downwind of the ridge crest (Figure 11).

4. Discussion

4.1. Influence of Radar Beam Height on Observed Reflectivity Patterns

As indicated in Figure 1, the height of the radar beam asl increases with increasing distance from the measurement device. For the transect shown in Figure 8 (T2), this results in a difference in measurement height of approximately 600 m along the transect, which might also affect the spatial distribution of particle concentration discussed. *Scipión et al.* [2013] compared the total snowfall amount of one season with the radar beam height and found a dependency with a correlation of $\rho = 0.6$, which correlates with the radar overshooting as winter precipitation often has limited vertical extension. Two arguments allow us to assume that the influence of the radar beam height does not drive the typical particle distribution observed by the radar.

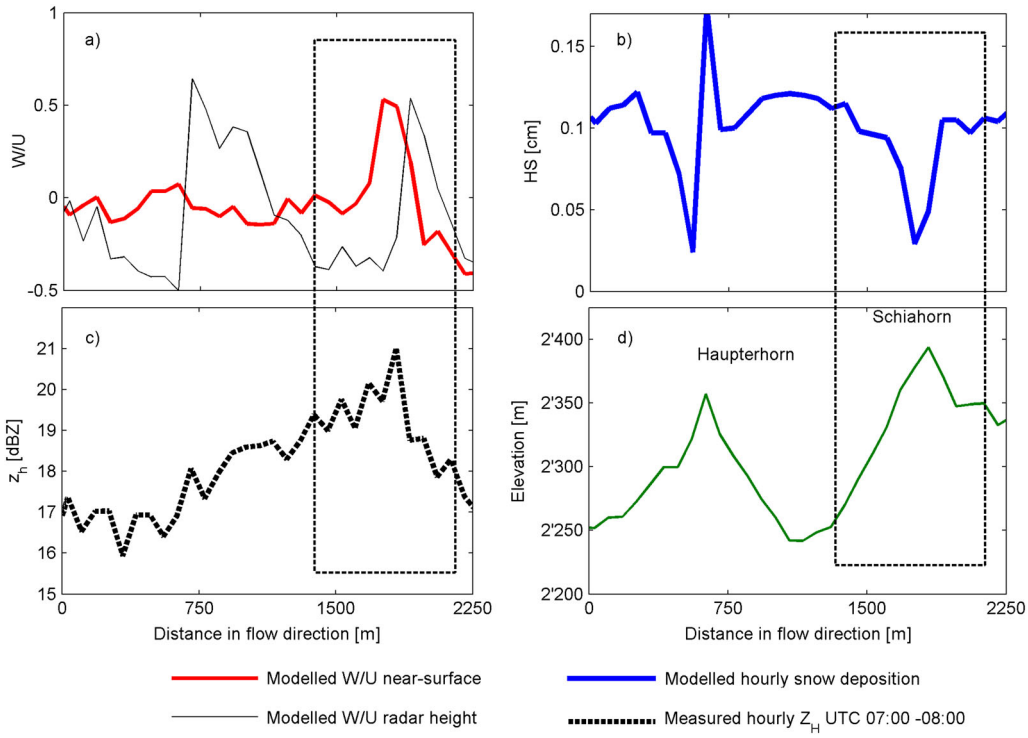

Figure 12. (a) Relation between surface-normal wind velocity (W) to horizontal wind velocities (U) (aspect ratio, W/U) are shown for the ground level and at the height seen by the radar. (b) Mean hourly radar reflectivity at horizontal polarization Z_H between 0700 and 0800 UTC on 17 March. (c) Modeled hourly snow deposition caused by preferential deposition of precipitation between 0700 and 0800 UTC on 17 March at Schiahorn (T2). (d) Topography. Location of transect T2 is shown in Figure 1.

First, ice water content typically decreases with altitude and with decreasing air temperature [*Hogan et al.*, 2006], leading to a decrease in radar reflectivity with decreasing altitude. Our measurements show a clear trend of increasing radar reflectivity on windward slopes with decreasing radar beam height, but a decrease in radar reflectivity is shown on leeward slopes, also with decreasing radar beam height. The increase of radar reflectivity on windward slopes is, however, much stronger than what the influence of temperature on the ice water content would be [*Hogan et al.*, 2006] for the corresponding height differences (e.g., around 400 m for T2). Second, the measurements further suggest that the effect of single mountain peaks on the precipitation field is independent of measurement height (Figure 8c).

4.2. Pure Particle-Flow Interaction at Low Atmospheric Levels

The purpose of this section is to answer the question "How is snow deposition at the ground affected by pure particle-flow interaction at lower atmospheric levels?" We therefore show quantities describing the mean flow field, the reflectivity field, and the modeled preferential snow deposition at the ground along transects in Figure 12. The aspect ratio W/U (Figure 12a) is the relationship between the surface-normal wind velocity (positive/negative) W and the mean horizontal wind velocity U. Modeled aspect ratios are illustrated for the ground level and for the height of the radar beam at the 9° level. Measured hourly Z_H at the 9° radar beam height and modeled preferential snow deposition governed by the near-surface flow field are compared in Figures 12b and 12c. Note that the model of preferential deposition of snow, as implemented in Alpine3D [*Lehning et al.*, 2008], only accounts for the effect of near-surface flow dynamics on the snow particle distribution in the air and snow deposition on the ground, assuming a spatially homogeneous precipitation input from above. The terminal velocity of snow particles is assumed to be constant. Furthermore, microphysical processes are not considered in the model.

The strongest updraft relative to horizontal wind speed (high aspect ratio) can be found approximately 50 m upwind the ridge crests of Haupterhorn and Schiahorn (Figures 12a and 7). Numerical simulations show that less snow is deposited on the upper windward slopes near the ridge crests as a result of an enhanced downstream advection of the snow particles due to a streamwise flow divergence (Figure 6c) and updrafts (Figure 12a). The location of the minimum snow deposition coincides with the location of the strongest

updraft. In contrast, if low horizontal advection (low horizontal wind speeds) coincides with downdrafts, particle trajectories converge and lead to enhanced snow deposition at this point of convergence. High negative aspect ratios were found some tens of meters downwind on the upper leeward slopes of the Haupterhorn and Schiahorn (Figure 12c). Streamwise convergence of hydrometeor trajectories further cause an abrupt reduction in the downstream advection of hydrometeors. Thus, streamwise flow convergence and high particle concentration appear to promote preferred deposition of snow on the upper leeward slopes, as was suggested by Alpine3D model runs (Figure 12c). Given the fact that flow deceleration on leeward slopes is likely dependent on the presence of a relatively weak static stability, preferred deposition of snowfall in leeward slopes is only possible if the atmosphere is slightly stably stratified. Higher stability would constrain the generation of flow separation and promote higher downslope winds. Additionally, higher stability would result in smaller differences in vertical velocity, and unstable situations are unlikely to occur close to the ground over snow. The simulated hourly snow deposition is also consistent with snow depth observations on the leeward slope of Chüpfenflue at the time of peak accumulation, which were attributed to preferred deposition of precipitation as was found in previous studies [*Mott et al.*, 2010, 2011].

Although neglected in the current model version, flow acceleration and updrafts would also reduce particle terminal velocity and would therefore increase the effect of preferential deposition of snow, thus leading to a stronger differentiation between the windward and the leeward snow deposition than could be seen from our current model (Figure 12c). The terminal velocity is smaller on upwind slopes and in updraft zones for two reasons:

1. The updrafts lead to a lower terminal fall velocity with respect to the Earth's surface simply because the flow is moving upward. If this is combined with a horizontal movement through the mean wind, there will be a net transport of particles from updraft zones to downdraft zones leading to less particle deposition below updraft zones. While close to the surface the wind has to be parallel to the terrain, this constraint quickly vanishes as one moves away from a (steeply) inclined surface.
2. In a turbulent flow with small time and length scales such as those close to the surface, the relative movement between particles and flow is large enough that a squared drag law applies to the particle acceleration from the fluid. As a result, particles get slowed down by turbulence when they approach the surface. Thus, the deposition velocity also depends on the turbulent kinetic energy, which is higher for the higher velocities found on the windward sides of mountain slopes. This leads to the fact that windward sides have lower terminal velocity than leeward slopes. The current model version based on mean flow fields cannot account for this second effect, however.

The modeled snow deposition fields are also consistent with the measured precipitation maxima (Figure 11), which indicated a considerable influence of wind velocity on the location of the snowfall maximum. Measurements showed that most precipitation maxima were found around the ridge crest and over the upper leeward slopes of the Schiahorn crest. The scatter of the data might be partly explained by the high dependency of the terminal velocity on particle size and the high radial velocities required to shift larger particles toward the leeward slopes. Additionally, a variety of additional multiscale orographic processes might have affected the spatial distribution of precipitation. How the interaction between microphysics with dynamical aspects of the flow might have affected the snowfall distribution is discussed in section 4.3. How the concentration field seen by the radar is connected to the modeled snow deposition field is discussed in section 4.4.

4.3. Interaction Between Microphysics With Dynamical Aspects of the Orographic Flow

4.3.1. Large-Scale Effects

The occurrence of rimed and/or aggregated crystals cannot be explained by buoyant convection since the large-scale flow was stable. What the measured vertical profiles of radial velocity above the Schiahorn ridge (Figure 4) and atmospheric soundings launched approximately 200 km west to the Davos region (Figure 3c) do indicate is the development of a shear layer between 3000 and 4000 m aboveground that potentially promoted mechanical turbulence at those layers. The strong shear evolved at approximately 0600 UTC over the region of Davos (Figure 4) and increased during the investigation period. The shear-induced mechanical turbulence potentially enhanced vertical air motions in the 3000–4000 m layer. Updrafts potentially raised moist air up to water saturation promoting precipitation formation [*Houze*, 2012; *Stoelinga et al.*, 2013] and could be an explanation for the area-wide increase in Z_H at this time of day and the joint occurrence of high Z_H and low Z_{DR} values at those elevations (Figure 10). As the strength of the wind shear increased during the investigated time period, the Z_H signal also increased (Figures 8 and 10), indicating enhanced precipitation

formation above the entire Davos region. Therefore, the evolution of a large-scale shear layer appears to affect the temporal evolution of snowfall rates at larger spatial scales.

4.3.2. Small-Scale Effects

As presented above, radar observations show clear small-scale spatial patterns of Z_H. The pronounced small-scale patterns of peak Z_H above the ridge crest could be either a sign of local microphysical processes or of the effect of the boundary layer flow on the particle trajectories. The combined analysis of horizontal and vertical distribution of Z_{DR} and Z_H, however, allows us to identify polarimetric signals which can be attributed to microphysical growth processes above the Schiahorn ridge.

In the morning, the low horizontal variability of differential reflectivity along the ridge between Schiahorn and Chüpfenflue (Figure 9b) is consistent with a homogeneous precipitation production with no strong lateral gradients in the properties of precipitation particles. This can also be interpreted as an indication of a rather uniform horizontal moisture and temperature distribution.

At 0500–1000 UTC on 17 March 2011, the high spatial variability of Z_{DR} signals measured at the same altitudinal range (e.g., over Schiahorn and Chüpfenflue summits) (Figure 9d) is assumed to be connected to differences in the processes behind precipitation particle formation. Considering the small width of the barrier Schiahorn (approximately 3 km), the advective time scale is much shorter than the conversion of condensates to precipitation and particle fallout. A local orographic cloud at this scale would be thus incapable of producing precipitation by itself [*Stoelinga et al.*, 2013]. A possible explanation for the coinciding small-scale spatial pattern of low Z_{DR} and high Z_H signals and the enhanced efficiency for precipitation production at a small area (Figures 9c and 9d) is that the orographically induced ascent of the airflow at low elevation produced a different condensation regime leading to low-level orographic cloud formation above the Schiahorn region. Low-level clouds in this region could have provided an additional moisture source for the growth of snow crystals falling from clouds advected at higher levels, thereby producing a higher Z_H signal close to the Schiahorn ridge. In the presence of a larger-scale seeding cloud aloft, low-level orographic clouds typically form similar small-scale patterns of positive/negative snowfall enhancement in the upwind/downwind region of summits [*Choularton and Perry*, 1986]. Further evidence of orographic snowfall enhancement above the ridge crest can be obtained by analyzing vertical profiles of Z_{DR} and Z_H above the summit region. Vertical Z_H and Z_{DR} profiles show low Z_{DR} and high Z_H signals at lower atmospheric layers. While the Z_{DR} signals increase with elevation, Z_H signals decrease with elevation. Both the concurrence of low Z_{DR} and high Z_H signals at lower atmospheric levels and their respective increasing/decreasing trend with elevation indicate the signature of crystals which grow by riming and aggregation [*Moisseev et al.*, 2009] at lower atmospheric layers. These types of crystals are typical for orographic enhancement of snowfall caused by the seeder-feeder mechanism [*Choularton and Perry*, 1986; *Dore and Choularton*, 1992]. Thus, reflectivity signals above Schiahorn at the 9° level scan appear to be strongly affected by the local formation of a feeder cloud. At higher atmospheric levels, no evidence of riming and aggregation can be found. These atmospheric levels are thus assumed to be above the feeder cloud.

Although increasing reflectivity in the downwind direction is observed over windward slopes for the time period 1500–2000 UTC, the horizontal analysis of Z_{DR} does not show rimed and/or aggregated crystals near the ridge crests (Figure 9f). Polarimetric signals after 1600 UTC show no significant layering of Z_H and Z_{DR} and thus indicate the presence of similar snow particle types, pointing to similar microphysical origins of snow particles for the whole vertical profile. Because of the limited spatial variability of Z_{DR} along the transect, the spatial variability of Z_H is supposed to reflect the spatial variability in particle concentration. One possible conclusion could be that snow particle concentration enhancement is not caused by microphysical processes (i.e., cloud dynamics) but is a result of the pure influence of the flow field on precipitation distribution as suggested by the concept of preferential deposition of precipitation established by *Lehning et al.* [2008]. An alternative explanation would be that a weaker seeder-feeder effect does not lead to strong riming of particles. The resulting pattern of reflectivity could thus be an additive effect of a weak precipitation enhancement over the ridge and an increase in particle density on the leeward slope caused by the particle-flow interaction, resulting in less pronounced peaks of reflectivity and a strong shift toward the leeward slopes in the presence of strong winds. The increase of mean Z_{DR} signals toward the lower leeward slope (Figure 8f) and the increase of Z_{DR} values with measurement height (Figure 10) would support this hypothesis.

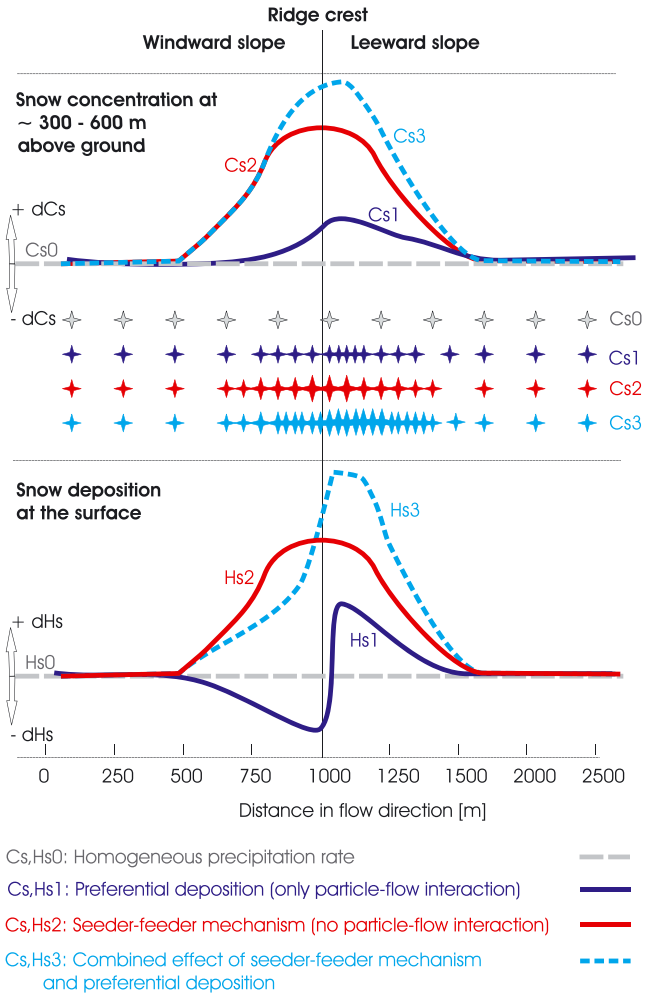

Figure 13. Hypothetical curves describing snow concentration (Cs) in the atmosphere (300–600 m aboveground) and snow deposition at the ground (Hs) for homogeneous precipitation (Cs0, Hs0), preferential deposition (Cs1, Hs1), seeder-feeder mechanism (Cs2, Hs2), and combined effect of preferential deposition and seeder-feeder mechanism (Cs3, Hs3). Stars indicate the particle concentration in the air.

A second alternative explanation for the local precipitation maxima above the Schiahorn ridge at 1500–2000 UTC would be the influence of small-scale cells of upward motion embedded within the larger-scale cross-barrier flow, which typically evolves for moist flows over small-scale ridges and valley [*Garvert et al.*, 2007; *Stoelinga et al.*, 2013]. The efficient microphysical conversion can be aided by small-scale terrain-induced or shear-induced cells of upward motions embedded within the larger-scale upward motion [*Stoelinga et al.*, 2013] leading to precipitation maxima over leeward slopes of smaller mountain ridges. Enhanced radial velocities above the ridges (Figure 6) and updraft/downdraft zones windward/leeward of the ridge (Figure 7) is consistent with the theoretical depiction of propagating mountain wave behavior, as discussed by *Garvert et al.* [2007].

4.4. Interaction Between Processes Driving Small-Scale Snowfall and Snow Deposition Patterns

Although both processes, snowfall enhancement due to the seeder-feeder mechanism and preferential deposition due to pure particle-flow interaction, would promote increased snowfall rates on leeward slopes (Figure 12), the two processes act at different atmospheric levels and probably scales. The seeder-feeder mechanism typically occurs at atmospheric levels hundreds of meters above the ground. The particle-flow interaction, in contrast, acts closer to the ground and typically over the entire depth of the atmospheric boundary layer. The strength of the impact of the boundary layer flow on particle trajectories strongly increases close to the surface. Consequently, the seeder-feeder mechanism may dominate the particle distribution at upper atmospheric levels (hundreds of meters above the ground) and preferential deposition of snowfall at atmospheric levels close to the ground (tens of meters above the ground). This assump-

tion is consistent with observed profiles of Z_{DR} signals, which are discussed above. Thus, both processes act together causing characteristic deposition features at the ground. Radar signals discussed in this study are, however, observed at atmospheric levels approximately 200–500 m above the ridge crest. While the seeder-feeder mechanism is assumed to be well detected by the radar, the radar signals might only reveal the alleviated signature of the preferential deposition of snow.

Figure 13 shows hypothetical curves describing the atmospheric snow concentration field (Cs) above the ridge crest at the radar measurement height and corresponding snow deposition at the ground (*Hs*) caused only by preferential deposition of precipitation (neglecting cloud formation processes), seeder-feeder mechanism (neglecting particle-flow interaction), and the combined effect of both processes. With constant seeding from above (pure particle-flow interaction), streamwise flow divergence and reduced snow deposition over the windward slope cause a slight increase of the particle concentration until the concentration reaches its maximum over the upper leeward slope, at the transition between streamwise flow divergence/convergence and reduced/enhanced snow deposition (Figure 13, Cs1). Streamwise flow convergence and enhanced snow deposition over the leeward side cause a gradual decrease in the particle concentration in the downwind direction. Since the influence of the topographically modified flow on particle trajectories increases close to the surface, the resulting snow deposition at the ground shows below average snow deposition on the windward side and a stronger amplification of particle accumulation on the leeward side of the ridge crest (Figure 13, Hs1). The hypothetical snow deposition curve is very similar to the modeled snow deposition curve above the Schiahorn (Figure 12c, marked area).

In the presence of a low-level feeder cloud the snowfall production is strongly enhanced above the ridge (Figure 13, Cs2). If advection effects caused by the horizontal wind are neglected, we would then expect a maximum snow deposition rate directly at the ridge crest and less snow deposition on windward and leeward slopes (Figure 13, Hs2). Such snow deposition patterns are, however, never observed in reality. More likely, the pure particle-flow interaction demonstrated by Cs1 is superimposed by the seeder-feeder mechanism resulting in a slight modification of Cs2 toward Cs3 (Figure 10). The peak is shifted downwind (Figure 11) toward the leeward slope owing to advection (Figure 13, Cs3). Although the location of the snowfall maximum would be similar to situations without snowfall enhancement, the peak snowfall rate is expected to be much higher owing to the additional snowfall production. Similarly, the snow deposition maximum is enhanced, and the area gaining enhanced snow deposition becomes larger (Figure 13, Cs3, Hs3).

In contrast to the described and modeled snow deposition fields (Figures 12c and 13, Hs1), the measured atmospheric snow concentration (Figure 12b) is already enhanced over the windward side and its maximum is located over the ridge crest and the upper leeward slope. The reflectivity signal thus show increased snow concentration over a larger distance than the small-scale snow deposition. The strong difference between snow concentration fields several hundreds of meters aboveground and the snow deposition at the ground is consistent with results shown by *Scipión et al.* [2013], who found large differences between seasonal snowfall patterns measured by the radar and seasonal snow accumulation patterns measured at the ground. They attributed this difference to wind-induced snow transport processes near the surface which also includes preferential deposition of snowfall.

The radar signals discussed in this study appear to reflect the interaction of both processes similar to Cs3 shown in Figure 13. Thus, the clear assignment of peak radar signals and snow deposition maxima to one of the two processes is challenging. The shape of the reflectivity curve strongly depends on the wind velocity and the type of particles. If the seeder-feeder mechanism dominates the particle distribution, rimed and aggregated snow particles are more likely to fall out than nonaggregated and unrimed crystals owing to their higher terminal velocities. Higher horizontal wind velocities are thus required to advect rimed and aggregated snow particles over the crest of a mountain range [*Houze and Medina*, 2005]. Thus, downstream advection of snow particles with the ambient wind appears to play a decisive role in the distribution of snowfall and snow deposition, as already suggested by numerical results of *Choularton and Perry* [1986], *Colle* [2004], and *Zängl* [2007a] and also confirmed by direct measurement results as shown above.

Consequently, for the case of a seeder-feeder mechanism,the location of the peak reflectivity signal does not necessarily coincide with the location of snow deposition maximum at the ground. Even if the reflectivity maximum is observed above the ridge, the near-surface flow field will cause a downwind drift of snow particles toward the leeward slope.

5. Conclusion and Outlook

In this study, we examined orographically induced small-scale snowfall patterns over Alpine terrain. In particular, we discussed the effect of orographic snowfall enhancement and of the particle-flow interaction on observed atmospheric snow concentration fields and the final snow deposition field at the ground. We compared the small-scale radar measurements of reflectivity and radial velocity at hundreds of meters aboveground with numerical results of the effect of the near-surface flow fields on the preferential deposition of snowfall at the ground.

At larger scales, the analysis of atmospheric soundings and profiles of polarimetric variables indicated the evolution of a shear layer that accompanied the passage of the frontal system with additional mechanical turbulence potentially generating enhanced precipitation rates at larger scales.

At smaller scales, polarimetric radar data analysis of a 20 h precipitation event showed temporally and spatially persistent patterns of Z_H and Z_{DR}. One pattern that was frequently observed by the radar is the joint occurrence of high Z_H and low Z_{DR} close to the summit which indicates the occurrence of rimed aggregate snowflakes and/or graupel at lower atmospheric levels. Additional information gained from vertical polarimetric profiles suggests that these patterns are consistent with a polarimetric signature of orographic enhancement of snowfall caused by the seeder-feeder mechanism. Alternatively, mountain wave propagation might have produced local precipitation maxima on the leeward slopes on the mountain ridge by generating small-scale terrain-induced cells of upward air motions.

Radar measurements also show a strong shift in the particle concentration maximum toward the leeward slopes for higher wind velocities. The location of the particle concentration maximum was shown to strongly correlate with the magnitude of the horizontal wind velocity. It was possible to demonstrate that downstream advection of snow particles with the ambient wind strongly affects the distribution of snowfall and snow deposition on the ground. Thus, reflectivity patterns observed by the radar can not be only attributed to the seeder-feeder mechanism. The modification of the snow concentration field from its typical distribution caused by seeder-feeder mechanism toward a distribution with a maximum snowfall over the leeward slope can only be explained by pure particle-flow interactions. We call the latter process, which describes the effect of the atmospheric boundary layer flow on the snow particle trajectories, the *preferential deposition of snowfall*.

Radar data supplemented by the numerical analysis of the flow field and snow deposition at the ground allowed us to demonstrate that orographic enhancement of snowfall typically occurred in regions of strong radial velocities and strong updrafts. We further presented arguments that mean horizontal and vertical wind velocities affect particle trajectories inducing reduced snow deposition rates on windward slopes and enhanced deposition on leeward slopes. Measurements thus show that small-scale precipitation patterns over single inner-alpine mountain peaks can differ significantly from those observed on a larger scale for large mountain ranges, where microphysical and dynamical trends tend to make the leeward slopes drier than windward slopes [*Houze*, 2012]. Overall, the following qualitative picture emerges: Terrain modifications of the wind field induce spatially varying snow deposition at the ground by two main processes: (i) Given the right temperature and moisture fields, sufficiently strong updrafts cause local feeder clouds above peaks and ridges, which then lead to large signals of enhanced snow deposition. (ii) The pure particle-flow interaction named preferential deposition is active in all cases of sufficient wind but produces a smaller differentiation in snow deposition. The preferred deposition on leeward slopes can thus be a result of just preferential deposition of snowfall or of the interaction between both processes. The radar signals presented in this study are influenced by both processes.

This also has an important implication on measuring small-scale precipitation patterns in alpine terrain. The location of maximum precipitation concentration was shown to vary over a 100 m range. Thus, current operational radar measurements, which typically have a resolution of 1 km or coarser [*Miniscloux et al.*, 2001; *Cosma et al.*, 2002], appear to be inadequate to explain the small-scale spatial variability of precipitation patterns in Alpine terrain. Moreover, they are often affected by significant ground clutter in mountainous regions.

The qualitative results of observed signatures need to be investigated in a more quantitative manner to fully understand the microphysical origins of snow particles and the relative importance of the local flow field

versus seeder-feeder mechanism on the observed peaks of snowfall over mountain peaks. This must be left to future work.

Area-wide snow depth measurements conducted before and after single snowstorm events would be necessary for a comparison between snow concentration fields at several hundreds of meters aboveground and the final snow deposition at the ground. Such a comparison would allow us to directly validate the concept of preferential deposition of precipitation as introduced by *Lehning et al.* [2008].

A more quantitative work could include the application of particle-identification algorithms [*Medina and Houze*, 2003] or a numerical analysis of microphysics [*Andrić et al.*, 2013], cloud formation processes, and particle trajectories during single precipitation events. Most mesoscale models available to date are, however, very limited in calculating atmospheric flows and cloud formation processes in steep terrain and at very high resolution [*Lundquist et al.*, 2012]. In this study, we only investigated the effect of flow field dynamics on the snowfall distribution. The question of how mean flow field characteristics affect the small-scale spatial distribution of rain will be also addressed in a future study.

The original description of preferential deposition [*Lehning et al.*, 2008], which describes the spatial variation of snow deposition as a function of the flow field-particle interactions is acting together with the advection of the maximum precipitation into the lee slope. The relative importance of these two processes cannot be quantified from the data analyzed in this study and will be subject to further research.

Acknowledgments

The work was funded by the Competence Center for Environment and Sustainability CCES (SwissEx Science and SwissEx) and by the Swiss National Science Foundation (grant 200021-125064 and grant 2000,21-125332). We thank Thomas Grünewald, Charles Fierz, and Matthew von Pokorny for their thoughtful comments, valuable discussions, and language editing. We thank Jakobshornbahn and in particular Vali Meier for their support during the radar measurement campaign. We also thank Jessica Lundquist and the anonymous reviewers who helped to improve the paper.

References

Anders, A. M., G. H. Roe, D. R. Durran, and J. R. Minder (2007), Small-scale spatial gradients in climatological precipitation on the Olympic Peninsula, *J. Hydrometeorol.*, *8*, 1068–1081.

Andrić, J., R. M. R. Kumjian, D. S. Zrnić, J. M. Straka, and V. M. Melnikov (2013), Polarimetric signatures above the melting layer in winter storms: An observational and modeling study, *J. Appl. Meteorol. Climatol.*, *52*, 682–700, doi:10.1175/JAMC-D-12-028.1.

Anquetin, S., F. Miniscloux, and J. D. Creutin (2003), Numerical simulation of orographic rainbands, *J. Geophys. Res.*, *108*, 8386, doi:10.1029/2002JD001593.

Bader, M. J., S. A. Clough, and G. P. Cox (1987), Aircraft and dual-polarization radar observations of hydrometeors in light stratiform precipitation, *Q. J. R. Meteorol. Soc.*, *113*, 491–515.

Bergeron, T. (1965), On the low-level redistribution of atmospheric water caused by orography, paper presented at International Conference on Cloud Physics, Tokyo.

Blanchet, J., C. Marty, and M. Lehning (2009), Extreme value statistics of snowfall in the Swiss Alpine region, *Water Resour. Res.*, *45*, W0524, doi:10.1029/2009WR007916.

Colle, B. (2004), Sensitivity of orographic precipitation to changing ambient conditions and terrain geometries: An idealized modelling perspective, *J. Atmos. Sci.*, *61*, 588–606.

Colle, B. A., R. B. Smith, and D. A. Wesley (2013), Theory, observations, and predictions of orographic precipitation, in *Mountain Weather Research and Forecasting, Springer Atmospheric Sciences*, edited by F. Chow et al., pp. 291–344, Springer Atmospheric Sciences.

Choularton, T. W., and S. J. Perry (1986), A model of the orographic enhancement of snowfall by the seeder-feeder mechanism, *Q. J. R. Meteorol. Soc.*, *112*, 335–345.

Clifton, A., and M. Lehning (2008), Improvement and validation of a snow saltation model using wind tunnel measurements, *Earth Surf. Proc. Land.*, *33*, 2156–2173.

Cosma, S., E. Richard, and F. Miniscloux (2002), The role of small-scale orographic features in the spatial distribution of precipitation, *Q. J. R. Meteorol. Soc.*, *128*, 75–92.

Dadic, R., R. Mott, M. Lehning, and P. Burlando (2010a), Wind influence on snow depth distribution and accumulation over glaciers, *J. Geophys. Res.*, *115*, F01012, doi:10.1029/2009JF001261.

Dadic, R., R. Mott, M. Lehning, and P. Burlando (2010b), Parameterization for wind-induced preferential deposition of snow, *J. Hydrol. Process.*, *24*, 1994–2006.

Dore, A. J., and T. W. Choularton (1992), Orographic enhancement of snowfall, *Environ. Pollut.*, *75*, 175–179.

Garvert, M. F., B. F. Smull, and C. F. Mass (2007), Multiscale mountain waves influencing a major orographic precipitation event, *J. Atmos. Sci.*, *64*, 711–737.

Groot Zwaaftink, C. D., H. Löwe, R. Mott, M. Bavay, and M. Lehning (2011), Drifting snow sublimation: A high resolution 3D model with temperature and moisture feedbacks, *J. Geophys. Res.*, *116*, D16107, doi:10.1029/2011JD015754.

Grünewald, T., and M. Lehning (2011), Altitudinal dependency of snow amounts in two small alpine catchments: Can catchment-wide snow amounts be estimated via single snow or precipitation stations?, *Ann. Glciol.*, *52*, 153–158.

Hogan, R. J., M. P. Mittermaier, and A. J. Illingworth (2006), The retrieval of ice water content from radar reflectivity factor and temperature and its use in evaluating a mesoscale model, *J. Appl. Meteorol. Climatol.*, *45*, 301–317, doi:10.1175/JAM2340.1.

Houze, R. A., and S. Medina (2005), Turbulence as a mechanism of orographic precipitation enhancement, *J. Atmos. Sci., IMPROVE Special Issue*, *62*, 3599–3623.

Houze, R. A. (2012), Orographic effects on precipitating clouds, *Rev. Geophys.*, *50*, RG1001, doi:10.1029/2011RG000365.

Kuhn, M. (2003), Redistribution of snow and glacier mass balance from a hydrometeorological model, *J. Hydrol.*, *282*, 95–103, doi:10.1016/S0022-1694(03)00256-7.

Lehning, M., H. Löwe, M. Ryser, and N. Raderschall (2008), Inhomogeneous precipitation distribution and snow transport in steep terrain, *Water Resour. Res.*, *44*, W07404, doi:10.1029/2007WR006544.

Lehning, M., T. Grünewald, and M. Schirmer (2011), Mountain snow distribution governed by elevation and terrain roughness, *Geophys. Res. Lett.*, *38*, L19504, doi:10.1029/2011GL048927.

Lundquist, K. A., F. K. Chow, and J. K. Lundquist (2012), An immersed boundary method enabling large-eddy simulations of flow over complex terrain in the wrf model, *Mon. Weather Rev.*, *140*, 3936–3955.

Medina, S., and R. A. Houze (2003), Air motions and precipitation growth in alpine storms, *Q. J. R. Meteorol. Soc.*, *129*, 345–372.
Minder, J. R., D. R. Durran, G. H. Roe, and A. M. Anders (2008), The climatology of small-scale orographic precipitation over the Olympic mountains: Patterns and processes, *Q. J. R. Meteorol. Soc.*, *134*, 817–839.
Miniscloux, F., J. D. Creutin, and S. Anquetin (2001), Geostatistical analysis of orographic rainbands, *J. Appl. Meteorol.*, *40*, 1835–1854.
Moisseev, D., E. Saltikoff, and M. Leskinen (2009), Dual-polarization weather radar observations of snow growth processes, paper presented at 34th Conference on Radar Meteorology, Williamsburg, VA, Amer. Meteor. Soc., 13B.2. [Available at http://ams.confex.com/ams/pdfpapers/156123.pdf.]
Mott, R., F. Faure, M. Lehning, H. Löwe, G. Michlmayr, B. Hynek, A. Prokop, and W. Schöner (2008), Simulation of seasonal snow cover development and seasonal snow cover distribution for glaciated sites (Sonnblick, Austrian Alps) with the ALPINE3D model, *Ann. Glaciol.*, *49*, 155–160.
Mott, R., and M. Lehning (2010), Meteorological modeling of very high resolution wind fields and snow deposition for mountains, *J. Hydromet.*, *11*, 934–949, doi:10.1175/2010JHM1216.1.
Mott, R., M. Schirmer, M. Bavay, T. Grünewald, and M. Lehning (2010), Understanding snow-transport processes shaping the mountain snow-cover, *The Cryosphere*, *4*, 545–559.
Mott, R., M. Schirmer, and M. Lehning (2011), Scaling properties of wind and snow depth distribution in an Alpine catchment, *J. Geophys. Res.*, *116*, D06106, doi:10.1029/2010JD014886.
Muth, X., M. Schneebeli, and A. Berne (2012), A sun-tracking method to improve the pointing accuracy of weather radar, *Atmos. Meas. Tech.*, *5*, 547–555.
Orlandini, S., and A. Lamberti (2000), Effect of wind on precipitation intercepted by steep mountain slopes, *J. Hydrol. Eng.*, *5*, 346–354.
Park, H. S., A. V. Ryzhkov, D. S. Zrnic, and K.-E. Kim (2009), The hydrometeor classification algorithm for the polarimetric WSR-88D: Description and application to an MCS, *Weather Forecasting*, *24*, 730–748.
Plummer, D. M., S. Göke, R. M. Rauber, and L. Di Girolamo (2010), Discrimination of mixed-versus ice-phase clouds using dual-polarization radar with application to detection of aircraft icing regions, *J. Appl. Meteor. Climatol.*, *49*, 920–936.
Purdy, J. C., G. L. Austin, A. W. Seed, and I. D. Cluckie (2005), Radar evidence of orographic enhancement due to the seeder feeder mechanism, *Meteorol. Appl.*, *12*, 199–206, doi:10.1017/S1350482705001672.
Rauber, R. M. (1987), Characteristics of cloud ice and precipitation during wintertime storms over the mountains of northern Colorado, *J. Climate Appl. Meteor.*, *26*, 488–524.
Rauber, R. M., L. O. Grant, D. Feng, and J. B. Snider (1986), The characteristics and distribution of cloud water over the mountains of Northern Colorado during wintertime storms. Part I: Temporal variations, *J. Clim. Appl. Meteor.*, *25*, 468–488.
Ryzhkov, A. V., and D. S. Zrnić (1998), Discrimination between rain and snow with a polarimetric radar, *J. Appl. Meteorol.*, *37*, 125–134.
Schättler, U., and C. Barbu (2010), Consortium for Small Scale Modelling (COSMO) Newsletter No. 10. Deutscher Wetterdienst, Offenbach am Main.
Schirmer, M., V. Wirz, A. Clifton, and M. Lehning (2011), Persistence in intraannual snow depth distribution: 1. Measurements and topographic control, *Water Resour. Res.*, *47*, W09516, doi:10.1029/2010WR009426.
Schneebeli, M., N. Dawes, M. Lehning, and A. Berne (2013), High-resolution vertical profiles of polarimetric X-band weather radar observables during snowfall in the Swiss Alps, *J. Appl. Meteorol. Climatol.*, *52*, 378–394.
Scipión, D. E., R. Mott, M. Lehning, M. Schneebeli, and A. Berne (2013), Seasonal small-scale spatial variability in alpine snowfall and snow accumulation, *Water Resour. Res.*, *49*, 1446–1457, doi:10.1002/wrcr.20135.
Shuur, T. J., A. V. Ryzhkov, P. L. Heinselman, D. S. Zrnic, D. W. Burgess, and K. A. Scharfenberg (2003), Observations and classification of echoes with the polarimetric WSR-88D radar, *Tech. Rep., Nat. Sev. Storm Lab. Rep.*, National Severe Storms Laboratory Rep. [Available at http://www.nssl.noaa.gov/88d-upgrades/WSR-88D_reports.html.].
Stoelinga, M. T., R. E. Stewart, G. Thompson, and J. M. Theriault (2013), Microphysical processes within winter orographic cloud and precipitation systems, in *Mountain Weather Research and Forecasting*, edited by F. Chow et al., pp. 345–408, Springer Atmospheric Sciences, doi:10.1007/978-94-007-4098-3_7.
Williams, E. R., et al. (2011), Dual-polarized winter storm studies supporting development of NEXRAD-based aviation hazard products, Extended Abstracts, paper presented at 35th Conference on Radar Meteorology, Amer. Meteor. Soc., Pittsburgh, PA.
Winstral, A., D. Marks, and R. Gurney (2013), Simulating wind-affected snow accumulations at catchment to basin scales, *Adv. Water Resour.*, *55*, 64–79.
Wolde, M., and G. Waldi (2001), Polarimetric signatures from ice crystals observed at 95 GHz in winter clouds, Part II: Frequencies of occurrence, *J. Atmos. Sci.*, *58*, 842–849.
Xue, M., K. K. Droegemeier, V. Wong, A. Shapiro, and K. Brewster (2001), The Advanced Regional Prediction System (ARPS)—A multi-scale non-hydrostatic atmospheric simulation model. Part II: Model physics and applications, *Meteorol. Atmos. Phys.*, *76*, 143–165.
Zängl, G. (2007a), Interaction between dynamics and cloud microphysics in orographic precipitation enhancement: A high-resolution modelling study of two north alpine heavy-precipitation events, *Mon. Weather Rev.*, *135*, 2817–2840.
Zängl, G. (2007b), Small-scale variability of orographic precipitation in the Alps: Case studies and semi-idealized numerical simulations, *Q. J. R. Meteorol. Soc.*, *133*, 1701–1716.
Zängl, G. (2008), The temperature dependence of small-scale orographic precipitation enhancement, *Q. J. R. Meteorol. Soc.*, *134*, 1167–1181.
Zängl, G., D. Aulehner, C. Wastl, and A. Pfeiffer (2008), Small-scale precipitation variability in the Alps: Climatology in comparison with semi-idealized numerical simulations, *Q. J. R. Meteorol. Soc.*, *134*, 1865–1880.